

Pore-scale Analysis of CO₂-brine Displacement in Berea Sandstone and Its Implications to CO₂ Injectivity

Guangyuan Sun*, Zhuang Sun, Andrew Fager and Bernd Crouse

Dassault Systèmes, San Francisco, USA

Abstract. For storage in deep saline formations, where CO₂ is injected into the pore spaces of rocks previously occupied by saline groundwater (brine), relative permeability is a key input parameter for predictive models. CO₂ injectivity is considered to reach the maximum value at the CO₂ endpoint relative permeability when brine saturation becomes irreducible. The objective of this study is to investigate the effect of viscosity ratio, interfacial tension and wettability on relative permeability during CO₂-brine drainage. A multiphase lattice Boltzmann model (LBM) is employed to numerically measure pore-scale dynamics in CO₂-brine flow in the sample of Berea sandstone. CO₂/brine with interfacial tension from 30 to 45 mN/m and viscosity ratio from 0.05 to 0.17 (the range of values expected for typical storage reservoirs conditions) are carried out to systematically assess the influence on the relative permeability curves. Although CO₂ storage in sandstone saline aquifers is predominantly water wet, there are contradictory results as to the magnitude of the contact angle and its variation with fluid conditions. Therefore, the range of wetting conditions is studied to gain a better insight into the effect of wettability on supercritical CO₂ displacement. In this study, it is observed that interfacial tension variations play a trivial impact while both of viscosity ratio and wettability are likely to have a significant effect on relative permeability curves under representative condition of storage reservoirs. We also perform a near-wellbore scale geomechanics analysis to investigate the impact of relative permeability on CO₂ injectivity. The result shows that water-wet condition facilitates the CO₂ injection when there is no fracture induced.

1 Introduction

It is well accepted that global warming is due to the increase in atmospheric concentrations of greenhouse gases, such as carbon dioxide (CO₂). To achieve mid- and long-term targets in reducing CO₂ emissions and their intensity, various mitigation approaches are explored, foremost among them being CO₂ capture, utilization and storage (CCUS), which will play a significant role in the first half of this century if reduction targets are to be met [1-2]. Current methods to reduce atmospheric emissions of anthropogenic greenhouse gases often include the capture of CO₂ and subsequent injection into deep subsurface formations [3-5]. Such injection scenarios involve multiple fluids and lead to multiphase flow problems. Common approaches involve injection of CO₂ into deep formations, such that the CO₂ will be under sufficiently high pressure and temperature to remain in a supercritical state. For temperatures T and pressures P above the critical point ($T_c = 31.1^\circ\text{C}$ and $P_c = 7.38\text{ MPa}$), the injected CO₂ will have significantly higher density than that of gaseous CO₂, although still less than that of the resident formation water, usually brine. The viscosity of the CO₂ is also significantly less than that of the brine. Therefore, migration of the CO₂ away from the injection well involves both gravity override and unfavorable mobility ratio.

The potential for CO₂ storage in saline aquifers largely depends on the storage capacity and the CO₂ injectivity of the site. The storage capacity of aquifers is governed by aquifer

volume, porosity, and, most importantly, volumetric as well as microscopic displacement efficiencies. Injectivity, on the other hand, is governed by permeability, relative permeability, fracture characteristics of the rock, and rock compressibility [6].

The primary independent variables on multiphase flow, other than the rock structure, are pressure, temperature and salinity. The fluid properties such as viscosity, density, contact angle and interfacial tension can be described as secondary variables, depending on the first ones. Relative permeability, irreducible water and residual CO₂ saturations may be considered as tertiary variables, as these are in turn controlled by the fluid properties [7].

The viscosity ratio is defined as the ratio of the viscosity of the non-wetting phase to the wetting phase. The effect of viscosity ratio on relative permeability is not clear, as the observations reported in the literature are contradictory. Relative permeability is shown to be both independent of [8] or to increase with viscosity ratio [9-11] in experimental oil/water systems. However, Lefebvre du Prey et al. [12] showed that for a high viscosity ratio, the relative permeability of the lower viscosity fluid significantly decreases during drainage. Downie and Crane [13] suggest that a subsequent decrease in viscosity ratio does not return the relative permeability to its original value, thus concluding that viscosity ratio is not the only factor to change relative permeability. Bachu and Bennion [7] found that an increase of interfacial tension or a decrease in the viscosity ratio brings about similar changes of relative permeability of brine, irreducible water and residual CO₂ saturations that is,

* Corresponding author: Guangyuan.SUN@3ds.com

increasing relative permeability and decreasing residual saturations.

Interfacial tensions for the CO₂-brine system typically range from 25 to 55 mN/m at the conditions for subsurface storage [14]. The data to investigate the effect of interfacial tension on relative permeability for the CO₂-brine system is limited. Bennion and Bachu [7] measured relative permeability curves of drainage and imbibition with interfacial tensions in the range 19.8 to 56.2 mN/m in a water-wet sandstone. Unlike the oil-brine system, a significant increase in permeability is observed for decreasing interfacial tension. The imbibition curves become more linear with decreasing interfacial tension, suggesting there is an increase in total relative mobility and the flow at low interfacial tension behaves miscible. Both endpoint permeability of CO₂ and residual CO₂ saturation increase as interfacial tension decreases. However, they also suggested that the effects of viscosity ratio and interfacial tension cannot be separated, as the viscosity ratio simultaneously increases (0.02, 0.05 and 0.1) as interfacial tension decreases (56, 34, 20 mN/m). The discrepancy about the influence of interfacial tension could potentially result from the low viscosity ratio of the CO₂-brine system ($\ll 1$) as opposed to the high viscosity ratio of the oil-water system ($\gg 1$) [15]. The oil-water system is much more strongly controlled by viscous forces, which have the effect of decreasing the influence of interfacial tension on distribution of the wetting and non-wetting fluids.

For CO₂ storage in sandstone saline aquifers, the reservoirs under consideration are expected to be predominantly water-wet [16-18] but the results are contradictory as to the magnitude of the contact angle and its variation with fluid conditions. Espinoza and Santamarina [16] observed that quartz and calcite in CO₂-brine system is strongly water-wet with no impact of changing pressure and a weak dependence on salinity up to 3.5M NaCl. Chiquet et al. [19] have also observed the system to be water-wet on quartz with little impact of both pressure and salinity from atmospheric up to 10 MPa pressure and for 0.01-1M NaCl solutions. However, a transition was observed from water- to intermediate-wet with increasing CO₂ pressure and NaCl and the system appeared to be mixed-wet across the entire range of conditions during imbibition. In microfluidic experiments with silica micromodels, Kim et al. [17] found contact angles ranging from water- to mixed-wet for the supercritical CO₂-brine system, as the salinity increases from 0.01 to 5M NaCl.

In this work, we present the results of a numerical study that carefully characterizes relative permeability of CO₂-brine in Berea sandstone using the steady-state method. We study the effect of key fluid properties (viscosity ratio, interfacial tension and wettability) on drainage displacement of brine by CO₂ injection at different flow conditions of reservoir. We also perform a near-wellbore scale geomechanics analysis to investigate the impact of relative permeability on CO₂ injectivity.

2 Measurements and procedure

In this section, we present detailed information regarding the rock sample, flow conditions, and simulation setup and procedure used in this study.

2.1 Micro-CT imaging and processing

A Berea sandstone sample was selected in the study. Micro-CT scans were carried out on a cylindrical core sample of 5 mm inch diameter and 10 mm inch length to acquire 3D images of the pore structure with resolution of 2.02 μ m/voxel. As the attenuation of X-rays within the sample are associated to the material density, the micro-CT scans provide grey-scale images with color values related to the sample material (Figure 1 left). The resulting 3D image was denoised using typical image processing techniques including contrast enhancement and low-pass filtering (Figure 1 middle). Threshold segmentation was applied resulting in a binary image (Figure 1 right) suitable to be used as input to the numerical simulations. The resolved porosity is 15.7% and an absolute permeability of 235 mD was obtained from single-phase flow simulation. An imaging domain of 500 \times 500 \times 500 voxels is chosen for the multi-phase flow simulations.

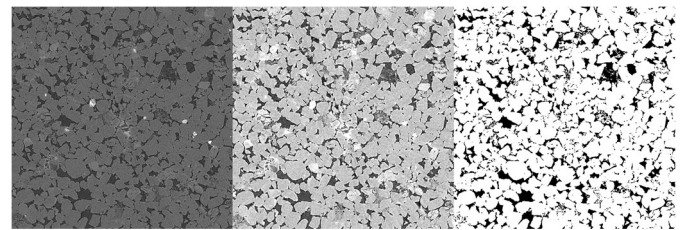


Fig. 1. Berea Sandstone micro-CT cross section: original (left), denoised (middle), and segmented (right) image slices.

2.2 Physical properties of system

To prepare for core flow condition, a primary drainage computation is performed to establish wettability distribution in pore space. It is assumed that during the drainage process, the smallest pores remain water-filled, while the non-wetting phase invades the remainder of the pore space. The pore surface can only become more repulsive to the water due to contact with non-wetting phase and the rock will achieve a “mixed wettability” state. More detail on these widely accepted mechanisms of aging or wettability alteration can be found in [20]. In the present numerical procedure, by assuming that 5% smallest pore volume still in contact with water after primary drainage, these pore surfaces are assigned a contact angle of 10°. The surfaces contacted by non-wetting phase are assigned a 30° and 170° contact angle for the water-wet and mixed-wet scenarios, respectively. The overall contact angle distributions are shown in Figure 2.

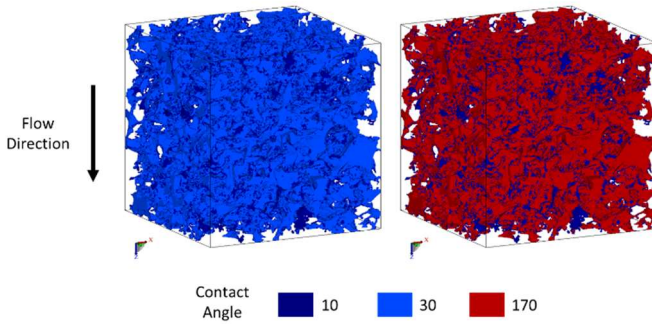


Fig. 2. Surface wettability in water- (left) and mixed-wet (right).

When it comes to fluid properties such as interfacial tension, viscosity and contact angle, it is straightforward to describe how these change with pressure, temperature and salinity. However, the design of a study to identify the individual contribution of each fluid property on the relative permeability remains a challenging exercise. As a result, the selections of fluid properties are at the same salinity (=1.98 mol/kg) and at the same time one or more of other parameters remain constant. It is common to use a dimensionless parameter such as capillary number (N_c) to combine these effects of interfacial tension and viscosity on relative permeability, which describes the ratio of viscous (governing flow) to capillary forces (governing trapping) acting in the pore space and is given by:

$$N_c = \frac{q\mu}{\sigma} \quad (1)$$

where q is the Darcy velocity, μ is the viscosity of the invading fluid and σ is the interfacial tension between CO₂ and brine. All the simulations reported in this study were performed under capillary dominated displacement regime with $N_c \sim 10^{-5}$ [21-22]. In section 3, the impact of the viscosity ratio, interfacial tension and wettability on relative permeability are discussed in more detail.

2.3 Multiphase numerical simulation

All flow simulations were performed using DigitalROCK™, which uses a numerical solver based on the Shan-Chen multi-phase lattice Boltzmann model [23]. This solver has been validated on a variety of fundamental benchmarks and real reservoir rock test cases [23-28]. It also includes the ability to deal with high viscosity ratio of the immiscible fluid phases [29].

A steady-state displacement method is applied to measure relative permeability in this work. A displacement simulation starts at initial 100% brine saturation. Once the simulation proceeds until total flow rate is converged, the permeability is measured. Then the mixture of CO₂ and brine with increased CO₂ fraction is injected until the certain CO₂ saturation level is reached. The injection stops and waits until the flow rate is converged to achieve the equilibrium. At this point the permeability of CO₂ and brine is measured again at the current saturation. The same process will be repeated until the residual condition is reached when the brine phase barely moves. Periodic boundary conditions and a driving force are

applied in the flow direction. Additional details for this method can be found in [22, 25].

3 Pore-scale numerical simulation results

3.1 Interfacial tension effect

The interfacial tension of the CO₂-brine system at conditions covering the range relevant to CO₂ storage has been recently measured with the most comprehensive dataset provided by Li et al. [14]. As a thermophysical property, the interfacial tension is a function of pressure, temperature, and brine salinity. At conditions in subsurface storage, the interfacial tension ranges from 55 mN/m at high temperature, low pressure and high salinity to 20 mN/m at low temperature, high pressure and low salinity. Therefore, when it comes to evaluating the impact of interfacial tension on multiphase flow in the CO₂-brine system, the multi-dimensional nature of the relevant parameter space (density, viscosity and interfacial tension) are changing over the conditions of pressure, temperature and brine salinity. By holding one or more of these parameters (viscosity ratio and density ratio) constant, three values of interfacial tension chosen are applied within the range from 30 to 45 mN/m (Table 1) to examine the effect of interfacial tension on relative permeability (Figure 3).

Table 1. Conditions of relative permeability curves to assess the effect of interfacial tension [14].

Subsurface condition		Thermophysical fluid property		
Pressure [MPa]	Temperature [°C]	Interfacial tension [mN/m]	Viscosity ratio [-]	Density ratio [-]
7	62	45	0.04	0.14
8	35	37	0.04	0.63
20	72	30	0.08	0.63

The results illustrate that the dependence of the relative permeability displacement characteristics (end-point saturation and shape) on interfacial tension under the certain range of conditions in storage reservoirs. Endpoint relative permeability to CO₂ during drainage decreases with increasing interfacial tension, and residual brine saturation increases with increasing interfacial tension. This confirms that for lower interfacial tension it should be easier for the non-wetting phase (CO₂) to pass through pore throats, leading to higher relative permeability. However, this suggests that variations in interfacial tension alone (for the range of conditions expected in storage reservoirs) are still little and will not lead to significant variation in the relative permeability characteristics of a given rock.

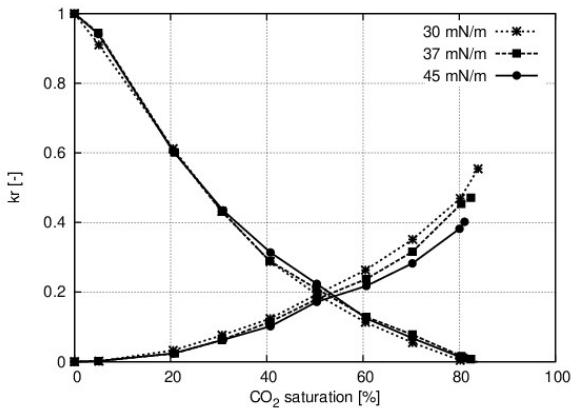


Fig. 3. Relative permeability curves measured for three different interfacial tensions.

3.2 Viscosity ratio effect

In this study, the viscosity ratio is defined as the ratio of the viscosity of CO₂ (non-wetting phase) to brine (wetting phase). CO₂ typically has lower viscosity than brine, and viscosity ratios from 0.02 to 0.2 are expected at geologically relevant conditions [30]. If injection of CO₂ into deep geological formations is considered, then the possible range of properties of the CO₂ can be estimated by considering typical conditions under which injection would occur. Because of the significant effect that the geothermal regime in a sedimentary basin has on CO₂-phase density and viscosity [31], we identify different basins in terms of magnitude of geothermal gradient and average land surface temperature. The average depth of the formation targeted for CO₂ storage range from about 1 km for shallow cold sites to 3 km for deep warm sites. Therefore, the properties of CO₂ and brine may vary, depending on pressure and temperature conditions. As representative condition of typical storage formations, surface temperature is 10 °C with geothermal gradient 25 °C/km for cold sites and 20 °C with geothermal gradient 45 °C/km for warm sites, respectively [30]. In both cases, a hydrostatic pressure gradient of 10.5 MPa/km is assumed that is typical for saline formation waters. Table 2 shows the conditions of pressure and temperature applied to study the effect of viscosity ratio. Under the conditions of deep cold formation, CO₂ injection is expected to be sufficiently deep to maintain the CO₂ in a supercritical state.

Table 2. Viscosity values for water and CO₂ at temperature (*T*) and pressure (*P*) conditions for representative deep old and shallow warm storage formation [30].

	Deep cold formation <i>P</i> : 31.5 MPa; <i>T</i> : 85 °C		Shallow warm formation <i>P</i> : 10.5 MPa; <i>T</i> : 65 °C	
	Viscosity [μPa·s]	Density [kg/m ³]	Viscosity [μPa·s]	Density [kg/m ³]
water	378	995	491	998
CO ₂	63	740	24	292
Ratio	0.17	0.74	0.05	0.29

Relative permeability curves of CO₂-brine with different viscosity ratios are shown in Figure 4. As the viscosity contrast between the two fluids increases, the less viscous fluid (CO₂) becomes more mobilized through the pore space and therefore has a higher permeability. This illustrates the advantage of deep aquifers that provides the injection conditions for CO₂ with higher mobility and thus more storage of CO₂.

Although it highlights that the individual effect of interfacial tension and viscosity ratio cannot be separated, interfacial tension does not play a significant role within certain storage conditions as suggested in this study. As seen previously, the interfacial tension for CO₂-brine systems decreases with increasing pressure and increases with increasing temperature and salinity. Water viscosity increases with pressure and salinity, and decreases with increasing temperature, while CO₂ viscosity also increases with pressure and decreases with increasing temperature. Considering that the variation of CO₂ viscosity is stronger than that of brine viscosity, the viscosity ratio of CO₂ to brine varies in the opposite manner as interfacial tension.

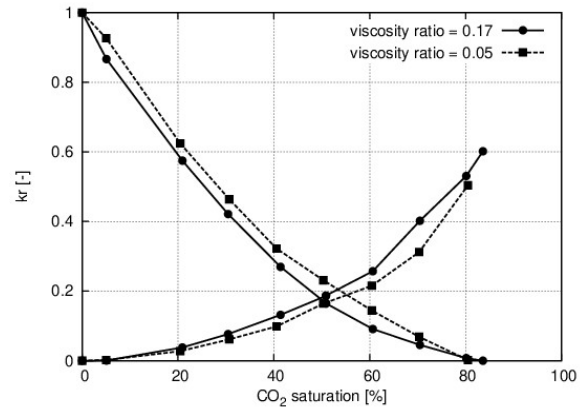


Fig. 4. Relative permeability curves measured for deep cold reservoir and shallow warm reservoir.

3.3 Wettability effect

Observations for CO₂-brine systems generally indicate a water-wet system for both sandstone and carbonate mineralogies, but there are contradictory results as to the magnitude of the contact angle and its variation with fluid conditions. In this study, two different wetting conditions (water-wet and mixed-wet) are chosen as defined in Section 2. The dependence of relative permeability on wetting condition are shown in Figure 5.

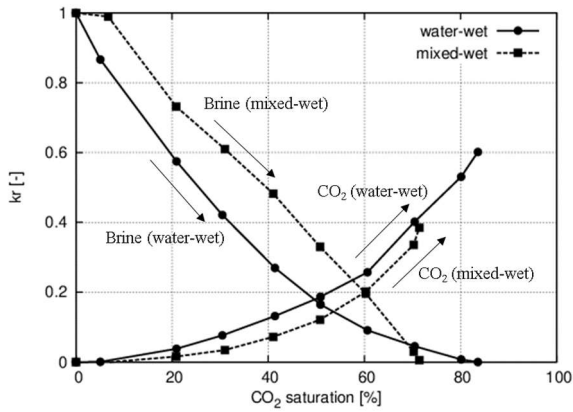


Fig. 5. Relative permeability curves measured for water-wet and mixed-wet condition.

During the displacement of water-wet system (drainage in this study), the rock is preferentially in contact with the water. As the nonwetting phase, CO₂ is generally located in the centers of the larger pores that forms continuous channels, while brine is found in the small pores and as a thin film on the rock surfaces. Eventually the remaining water is mainly found in three forms: (1) filling the smaller pores, (2) as a continuous film over the pore surface and (3) as trapped blobs surrounded by CO₂. In a mixed-wet system, the location of the two phases is reversed from the water-wet case. The injected CO₂ tends to imbibe into small and medium size pores, moving water into the large pores where it is easily displaced. The disconnected residual water remains in two forms: (1) small blobs in the centres of the larges pores, and (2) larger patches of water that are completely surrounding by CO₂. As above observed, the residual fluid distribution is shown in Figure 6.

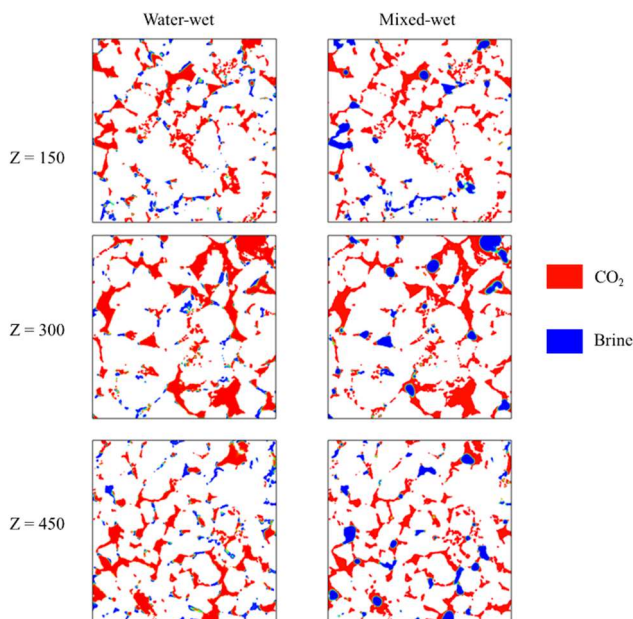


Fig. 6. Fluid distribution (red: CO₂; blue: brine) at residual stage along different depth in flow direction (Z) (left: water-wet; right: mixed-wet).

The differences in the relative permeability measured in water-wet and mixed-wet systems are caused by the differences in the fluid distributions. Consider a water-wet system, the brine does not significantly block the flow of CO₂, and the CO₂ permeability is relatively higher. This leads to a more efficient displacement than the one in a mixed-wet system and consequently lower residual water saturation. In contrast, the positions of the two fluids are reversed in mixed-wet system, CO₂ permeability is lower and brine permeability is higher because CO₂, as the wetting phase, tends to be located in the small pores and as a film on the surface, where it has little effect on the water flow. Therefore, the results of different wettability indicate that in CO₂-brine system, water-wet formation is able to store more CO₂ and more efficient injection is observed.

4 Near-wellbore analysis of CO₂ injectivity

We have shown the impact of wetting condition on the relative permeability curve in Section 3. In this section, we further perform a near-wellbore geomechanics analysis to investigate how the wettability impacts the CO₂ injectivity. The injectivity measures the ability of an injection well to receive injected fluid, and is a key parameter of CO₂ storage. It is defined as $II = q_i / \Delta P$, where II is the injectivity index, q_i is the injection rate, and ΔP is the pressure drop (bottom hole flowing pressure – reservoir pressure). CO₂ injectivity is considered to reach the maximum value at the CO₂ endpoint relative permeability when brine saturation becomes irreducible.

We set up the geomechanics model based on the finite element solver AbaqusTM. The porous formation is assumed isotropic and poroelastic following the Biot's theory [32]. Fluid flow in the pore space follows the Darcy's law. Governing equations of deformation and pore fluid flow are based on well-established theories and can be found in many textbooks and literatures [33-35]. Therefore, they are not repeated in this study.

A large CO₂ injection rate may induce fractures near the wellbore (e.g. In Salah CO₂ storage project) [36]. We model the fracture propagation and fluid flow in the fractures based on the cohesive zone method (CZM). CZM characterizes the fracturing process as the damage evolution between two initially bonded surfaces with zero thickness, and has been widely used in fracture mechanics. Detailed description of the CZM can be found in the Abaqus Documentation and many other literatures [37].

Figure 7 shows a schematic of the geomechanics model. We adopt a plane strain model (zero strain in the direction normal to the plane, a typical assumption for near-wellbore fracturing process) with a maximum principal stress σ_{max} of 20 MPa and a minimum principal stress σ_{min} of 10 MPa. We assign no normal displacement conditions to all the boundaries. The domain size is 50 × 50 m and the injection well is located in the center of the domain.

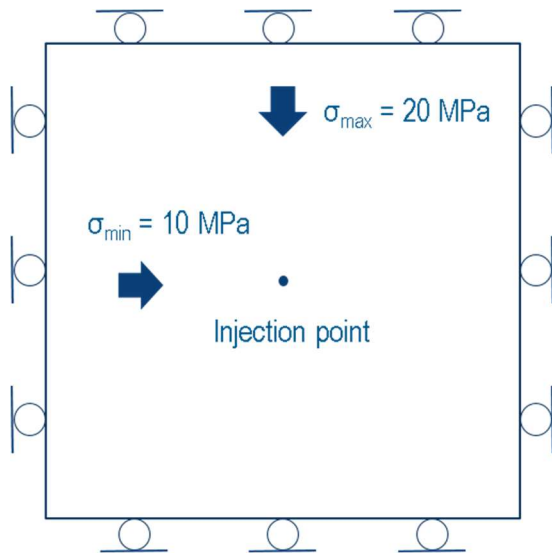


Fig. 7. Schematic of the geomechanics model. Domain size: 50 × 50 m.

In this section, we focus on the impact of wettability on the CO₂ injectivity. We consider two scenarios: water-wet and mixed-wet as presented in Section 3. Table 3 summarizes the geomechanics model parameters. The wetting condition will impact the relative permeability curve. All other parameters remain identical for these two case scenarios.

Table 3. Parameters of the geomechanics model

Parameters	Water-wet	Mixed-wet
Permeability (mD)	235	
Porosity	15.7%	
Residual water saturation (S_{wr})	16.4%	28.6%
Effective permeability of CO ₂ at S_{wr} (mD)	141.1	90.4
Young's modulus (GPa)	15	
Poisson's ratio	0.25	

We perform a baseline simulation with a CO₂ injection rate of 0.1 m³/s, water-wet condition. Figure 8 shows geomechanics simulation results including the pore pressure distribution at 100 s, the horizontal stress distribution at 100 s, and the evolution of injection pressure. CO₂ injection induces a fracture propagating perpendicular to the minimum principal stress direction. The injection pressure finally becomes stable at ~ 20 MPa.

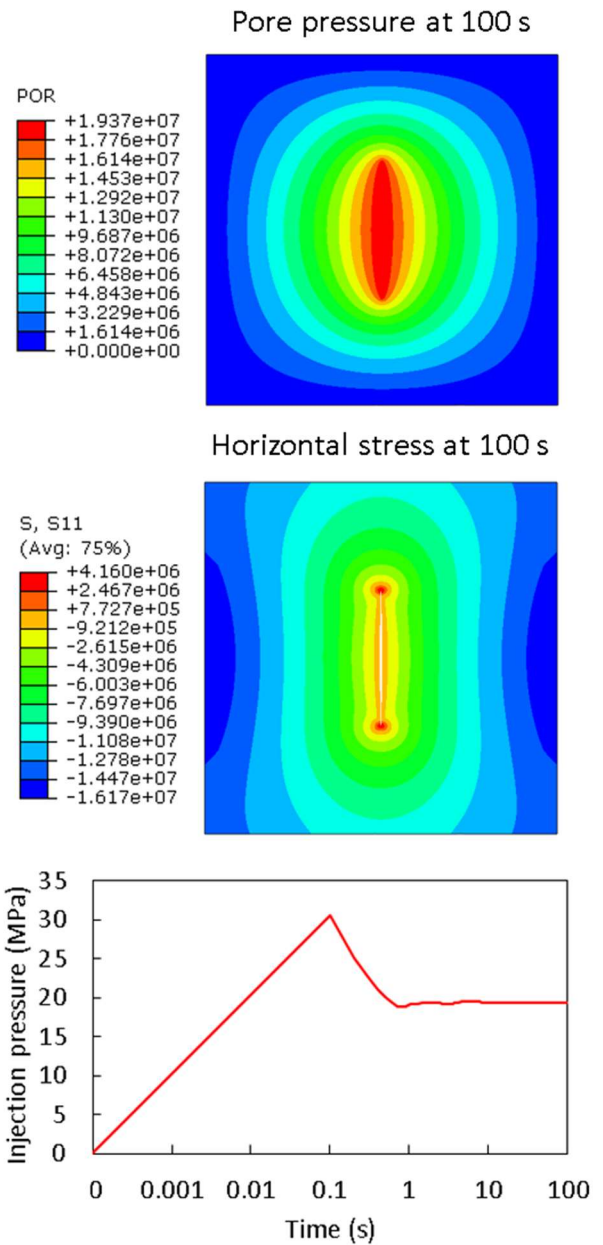


Fig. 8. Top: pore pressure distribution at the end of the numerical simulation (100 s). Middle: horizontal stress distribution at the end of the numerical simulation (100 s). Bottom: change of injection pressure over time. Time is plotted in a log scale to facilitate the visualization of pressure change. The injection pressure stabilizes at ~ 20 MPa. CO₂ injection rate is 0.1 m³/s and it is a water-wet condition.

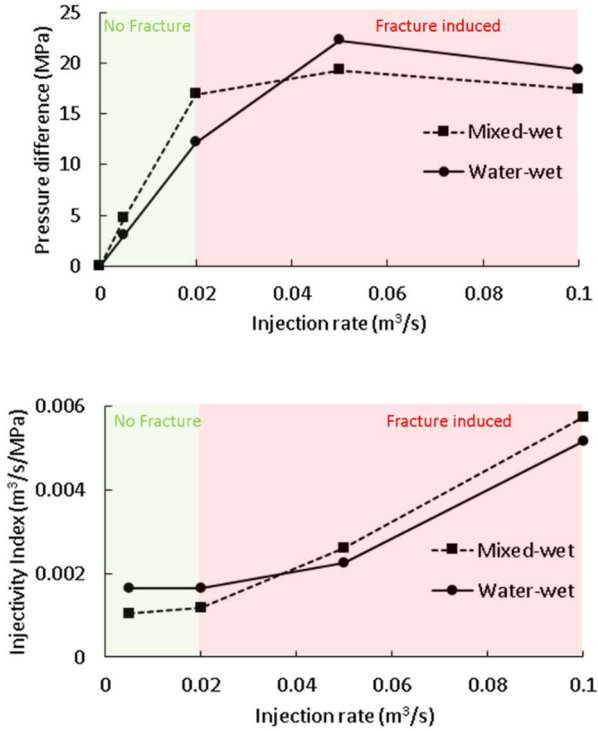


Fig. 9. Effect of wettability on CO₂ injectivity. The bottom figure is calculated from the top figure, where the injectivity index is defined as the injection rate over the pressure difference.

Figure 9 shows the geomechanics simulation results by varying the wetting condition and the injection rate. Each point corresponds to one geomechanics simulation. All other parameters remain identical. When the injection rate is relatively low (≤ 0.02 m³/s), there is no fracture and the fluid flow follows the Darcy's law. On the contrary, when the injection rate is high, a fracture is induced and the injectivity is significantly enhanced (manifested as a change in slope in the pressure difference - injection rate curve). Nevertheless, the induced fracture on the other hand may compromise the CO₂ containment, therefore, it is typically not favorable during a CO₂ injection.

We simulate two wetting conditions: water-wet and mixed-wet as discussed in Section 3. Water-wet condition facilitates the CO₂ fluid flow by offering the large pores and continuous flowing channels, which exhibits as a higher relative permeability of CO₂ on the relative permeability curve. Therefore, water-wet condition tends to have a higher injectivity compared to the mixed-wet condition when the injection rate is relatively low (no induced fracture). On the other hand, mixed-wet condition of a low CO₂ relative permeability facilitates the fracturing process. Therefore, mixed-wet condition tends to have a higher injectivity compared to the water-wet condition when the injection rate is high (with induced fracture), which indicates that the induced fracture starts to dominate the injectivity behavior. In summary, the wetting condition has an opposite impact on the CO₂ injectivity before and after the fracture was induced. Given that CO₂ injection generally tends to avoid fracturing process near the wellbore, a water-wet condition would be preferred from an injectivity perspective.

5 Conclusion

Using a DigitalROCK simulation approach, numerical simulation was carried out in Berea sandstone sample to study the impact of fluid properties (interfacial tension, viscosity ratio, and wettability) on steady-state relative permeability. As all these fluid properties depend on temperature, pressure and salinity, isolating the independent impact of them on relative permeability needs to hold one or more of other parameters constant. A weak dependency of displacement characteristics (end point relative permeability and shape of relative permeability and residual brine saturation) on interfacial tension was observed within typical range of storage formation condition. In contrast, viscosity ratio between CO₂ and brine shows clear dependency. Endpoint relative permeability to CO₂ decreases with increasing interfacial tension and decreasing viscosity ratio, while residual brine saturation increases with increasing interfacial tension and decreasing viscosity ratio. As it is common to consider storage formation as water-wet and the variation of contact angle observed in previous experiments, different wettability (water-wet and mixed-wet) are explored to investigate its impact on relative permeability. It turns out that the wettability has strong influences on relative permeability and there will be more CO₂ injected with higher CO₂ mobility in water-wet condition. A near-wellbore geomechanics model further demonstrates that a water-wet condition is preferred from an injectivity perspective.

References

1. IEA (International Energy Agency) Prospects for CO₂ Capture and Storage. IEA/OECD, Paris, 249 (2004)
2. IPCC (Intergovernmental Panel on Climate Change) IPCC special report on carbon dioxide capture and storage. In: Metz B, Davidson O, de Coninck HC, Loos M, Mayer LA, Cambridge University Press, Cambridge, 442 (2005)
3. S. Bachu, J. J. Adams, Energy Conversion and Management **44**(20), 3151-3175 (2002)
4. S. Holloway, Annual Review of Energy and the Environment **26**, 145-166 (2001)
5. S. M. Klara, R. D. Srivastava, and H. G. McIlvried, Energy Conversion and Management **44**, 2699-2712 (2003)
6. Y. Cinar, A. Riaz, & H. A. Tchelepi, SPE Journal, **14**(04), 588-594 (2009)
7. S. Bachu, B. Bennion, Environmental Geology, **54**(8), 1707-1722 (2008)
8. M.C. Leverett, Transactions of the AIME, **132**(1), 149-171 (1939)
9. S. T. Yuster, Proceedings of the 3rd World Petroleum Congress, **2**, 437-445 (1951)
10. A. S. Odeh, Trans., AIME, **216**, 346-353 (1959)
11. R. Ehrlich, Transport in Porous Media, **11**(3), 201-218 (1993)
12. E. J. Lefebvre du Prey, Society of Petroleum Engineers Journal, **13**(01), 39-47 (1973)

13. J. Downie, F. E. Crane, Society of Petroleum Engineers Journal, **1(02)**, 59-60 (1961)
14. X. Li, E.S. Boek, G.C. Maitland, J. M. Trusler, Journal of Chemical & Engineering Data, **57(5)**, 1369-1375 (2012)
15. B. Bennion, S. Bachu, SPE/DOE Symposium on Improved Oil Recovery, 1-10, January (2006)
16. D.N. Espinoza, J.C. Santamarina, Water Resources Research, **46**, 7 (2010)
17. Y. Kim, J. Wan, T.J. Kneafsey, T.K. Tokunaga Environmental Science and Technology, **46 (7)**, 4228-4235 (2012)
18. J. W. Jung, J. Wan, Energy & Fuels, **26**, 6053-6059 (2012)
19. P. Chiquet, J.L. Daridon, D. Broseta, S. Thibeau, Energy Conversion and Management, **48**, 736-744 (2006)
20. J. S. Buckley, Y. Liu, S. Monsterleet, Society of Petroleum Engineers Journal, **3(01)**, 54-61 (1998)
21. R. Xu, B. Crouse, D.M. Freed, et al. SCA **2018-066** presented at at the International Symposium of the Society of Core Analysts held in Trondheim, Norway (2018)
22. A. Fager, G. Sun, R. Xu, et al. Journal of Petroleum Science and Engineering, **208**, 109435 (2022)
23. X. Shan, H. Chen, Physical Review E, **47(3)**, 181 (1993).
24. B. Crouse, D. M. Freed, N. et al. SCA **2016-058** presented at the International Symposium of the Society of Core Analysts held in Snow Mass, Colorado, USA (2016)
25. G.R. Jerauld, J. Fredrich, N. Lane, Q. Sheng, B. Crouse, D. M. Freed, R. Xu, In SPE Abu Dhabi International Petroleum Exhibition & Conference. Society of Petroleum Engineers. November (2017)
26. H. Otomo, H. Fan, Y. Li, M. Dressler, I. Staroselsky, R. Zhang, H. Chen, Journal of Computational Science, **17**, 334-339 (2016)
27. H. Chen, C. Teixeira, K. Molvig, International Journal of Modern Physics C, **9(08)**, 1281-1292 (1998)
28. X. Shan, X.F. Yuan, H. Chen, Journal of Fluid Mechanics, **550**, 413-441 (2006)
29. H. Otomo, B. Crouse, M. Dressler, D. M. Freed, I. Staroselsky, R. Zhang, Chen, H, Computers & Fluids, **172**, 674-682 (2018)
30. J. M. Nordbotten, M. A. Celia, and S. Bachu, Transport in Porous Media, **58(3)**, 339-360 (2005)
31. S. Bachu, **Environmental** Geology, **44**, 277-289 (2003)
32. M.A. Biot, The Journal of the acoustical Society of america, **28(2)**, 179-191 (1956)
33. Jaeger, John Conrad, Neville GW Cook, Robert Zimmerman. *Fundamentals of rock mechanics* (John Wiley & Sons, 2009)
34. Zienkiewicz, Olgierd C., et al. *Computational geomechanics*, Vol. 613 (Chichester: Wiley, 1999)
35. E. Detournay, A.H.D. Cheng, *Fundamentals of poroelasticity*. In Analysis and design methods, 113-171 (Pergamon. 1993)
36. P. S. Ringrose, A. S. Mathieson, I. W. Wright, F. Selama, O. Hansen, R. Bissell, N. Saoula, and J. Midgley, Energy Procedia **37**, 6226-6236 (2013)
37. Abaqus. 2021. Abaqus 2021 online documentation.